

# Identifying atmospheric fronts based on diabatic processes using the dynamic state index (DSI)

Laura Mack<sup>1,2\*</sup>, Annette Rudolph<sup>2,3</sup> and Peter N vir<sup>2</sup>

<sup>1</sup>Department of Geosciences, University of Oslo, Oslo, Norway.

<sup>2</sup>Institute of Meteorology, Freie Universit t Berlin, Berlin, Germany.

<sup>3</sup>Institute of Landscape Architecture and Environmental Planning,  
Technical University Berlin, Berlin, Germany.

\*Corresponding author(s). E-mail(s): [laura.mack@geo.uio.no](mailto:laura.mack@geo.uio.no);

## Abstract

Atmospheric fronts are associated with precipitation and strong diabatic processes. Therefore, detecting fronts objectively from reanalyses is a prerequisite for the long-term study of their weather impacts. For this purpose, several algorithms exist, e.g., based on the thermic front parameter (TFP) or the F diagnostic that combines relative vorticity and horizontal temperature gradient. It is shown that both methods have problems to identify weak warm fronts since they are characterized by low baroclinicity. To avoid this inaccuracy, a new algorithm is developed that considers fronts as deviation from an adiabatic and steady state. These deviations can be accurately measured using the dynamic state index (DSI). The DSI shows a coherent dipole structure along fronts and is strongly correlated with precipitation sums. Using the DSI, a new front detection algorithm is developed (called DSI method), which allows to clearly identify the global storm track regions. The properties of the identified fronts depend on the applied front detection method, whereby fronts identified with the DSI method have particularly high specific humidity. Using a simple estimate for front speed, it is shown that also the front speed depends on the front detection method and that fronts identified using the DSI method have a higher front speed than fronts identified with the TFP method. This can be attributed to the dipole structure of the DSI and thus demonstrates the potential of the DSI to inherently indicate the movement speed and direction in atmospheric flows.

**Keywords:** Objective Front Identification, Front Detection, Front Climatology, Diabatic Processes, Dynamic State Index

# 1 Introduction

Fronts are air mass boundaries, that occur as far-reaching features from extra-tropical cyclones (Catto and Pfahl, 2013) and are associated with weather extremes, such as strong precipitation, wind gusts or compound extreme events (Catto et al, 2012; Catto and Pfahl, 2013; Clark and Gray, 2018; Raveh-Rubin and Catto, 2019). Catto and Pfahl (2013) showed that globally 51% of precipitation extremes occur along fronts and in storm track regions even 90%. With climate change, frontal activity is expected to shift poleward and to decrease in the northern hemisphere accompanied by a decrease in front-associated precipitation (Berry et al, 2011; Catto et al, 2014; Dagon et al, 2022). The general increase in specific humidity in a warmer atmosphere is thereby altered non-linearly and spatially inhomogeneously by atmospheric dynamics (Pfahl et al, 2017).

Fronts separate different air masses (Bjerkness and Solberg, 1922) and manifest themselves as band-like hyper-baroclinic zones (Renard and Clarke, 1965), which initially form due to geostrophic deformation (Hoskins, 1982). Since the front-parallel component falls within the synoptic-scale, while the front-perpendicular component falls within the meso-scale (i.e. relative vorticity and Coriolis parameter are of the same magnitude), fronts are a cross-scale phenomenon and theoretically described in a semi-geostrophic Eulerian framework (Hoskins, 1982). The coupling between temperature and wind field induces a cross-frontal ageostrophic secondary circulation, which further amplifies the horizontal temperature gradient (Sawyer, 1956; Eliassen, 1962) and causes a pronounced area of minimum pressure and maximum relative vorticity along the front (Hoskins, 1982). The development of fronts can be diagnostically analyzed with a frontogenesis function (Pettersen, 1936) or studied based on the isentropic slope tendency that accounts for the opposing effects of diabatic heating and tilting of isentropic surfaces (Papritz and Spengler, 2015). Alternatively, a Lagrangian view of fronts allows to consider different conveyor belts as coherent air streams around cyclones (Wernli and Davies, 1997). The complex dynamical processes along fronts cause various scale interactions, with larger-scale cyclones and meso-scale convection. The relation between fronts and cyclones is subject of a cause-and-effect discussion with two points of view (Schemm and Sprenger, 2018): According to the Bergen school (Bjerkness and Solberg, 1922) cyclones develop at the polar front when it becomes unstable, such that northward moving warm air forms a warm front downstream and southward moving cold air a cold front upstream. This type of cyclone is called initial-front cyclone and usually forms over the western oceanic boundary currents (Schemm and Sprenger, 2018). The theory of baroclinic instability explains the formation of cyclones from a broad hyper-baroclinic zone (Charney, 1947; Eady, 1949), and fronts can then form as consequence of the cyclogenesis process. These cyclones – referred to as late-front cyclones – predominantly form orographically in the lee of large mountain ridges (Schemm and Sprenger, 2018).

In particular cold fronts play an important role in the initiation of convective cells (Markowski and Richardson, 2010), which was recently systematically studied in a cell-front distance framework by Pacey et al (2023). Attributing weather events to fronts thus requires to distinguish their contribution from cyclones and meso-scale phenomena (Rudeva and Simmonds, 2015), which calls for automated front detection

procedures (Hewson, 1998).

Due to this complex multi-scale nature of frontal dynamics, diagnostic data-based studies that analyze climatologies and characteristics of fronts statistically from reanalyses or climate projections are of central importance (e.g. Berry et al, 2011; Simmonds et al, 2011; Catto and Pfahl, 2013; Catto et al, 2014; Parfitt et al, 2017; Bochenek et al, 2021; Dagon et al, 2022; Niebler et al, 2022; Pacey et al, 2023) – and the basis for these studies are methods for front identification. Hewson (1998) pointed out the advantages of automated and reproducible algorithms for front identification, which are referred to as 'objective' methods, compared to hand-drawn front lines on weather maps, which are referred to as 'subjective' methods (Uccellini et al, 1992). According to Hewson (1998), 'objective' methods should be simple, intelligible, accurate, tunable and portable. But even for these 'objective' methods, suitable meteorological variables and threshold values must first be found. Due to the diverse properties of fronts, which cannot always be unambiguously assigned to fronts only (Thomas and Schultz, 2019), various criteria can be designed for this purpose that focus on different characteristics of fronts.

Renard and Clarke (1965) consider fronts as a hyper-baroclinic zone with a pronounced thermal gradient that separates two air masses of less baroclinicity and thus motivates them to introduce the thermal front parameter (TFP) as gradient of horizontal baroclinicity to detect atmospheric fronts threshold-based from gridded data (Hewson, 1998). The thermal front parameter can be calculated based on different thermal quantities, such as temperature (Serreze et al, 2001), potential temperature (Berry et al, 2011), equivalent potential temperature (Schemm et al, 2015) or wet-bulb potential temperature (Catto et al, 2014) (of which the last two also take humidity into account). Simmonds et al (2011) introduced a front identification method based on a dynamical quantity only, by detecting surface fronts based on a 10 m-wind shift. Parfitt et al (2017) combines the horizontal temperature gradient as thermal quantity with the relative vorticity as dynamical quantity to one detection variable, called F diagnostic. However, these different detection methods lead to differences in global front climatologies, their seasonal variability and the attribution of precipitation to them (Hope et al, 2014; Schemm et al, 2015; Soster and Parfitt, 2022), which makes it difficult to draw generally valid and reproducible conclusions on these questions.

This is why we provide a new alternative view on front detection: We consider fronts as deviation from a stationary, adiabatic and inviscid basic state. This basic state can be exactly derived from the primitive equations and the deviation from it is measured with the dynamic state index (DSI) (Névir, 2004; Weber and Névir, 2008). In the basic state the DSI equals zero, while along fronts strong deviations occur, which are related to ongoing unsteady and diabatic processes associated with latent heat release and precipitation (Claussnitzer et al, 2008).

Our aim is to apply the DSI to front detection by developing a new DSI-based front detection algorithm ("DSI method") and compare it in both, a case study and a global climatology, with existing front detection methods and discuss differences in the properties of the detected fronts. With this new DSI method, our study contributes to the discussion about front detection methods, which are the fundamental basis for diagnostic studies investigating the properties, dynamics, scale interaction and weather

impact of fronts.

The study starts with recapitulating two existing front identification methods (utilizing TFP and F diagnostic, Sec. 2) based on a case study. Then, the DSI is introduced and it is shown how the DSI reflects fronts. Based on this, the new front identification method ("DSI method") is developed (Sec. 2.5). Sec. 3 compares the three methods based on a global climatology and their annual cycle using ERA5, and examines which properties the detected fronts have.

## 2 Data and Methods

### 2.1 Approaches for identifying atmospheric fronts

Since fronts separate air masses with different thermal properties, they are characterized by a strong horizontal temperature gradient. In the classical Bergen cyclone model (Bjerknes, 1919; Bjerknes and Solberg, 1922) fronts were understood as zero-order discontinuity in the temperature field, which is until today the motivation for weather services to draw fronts as lines in weather maps. However, this view on fronts violates the basic continuity principle of fluid dynamics (e.g. Tao et al, 2014), so it has been revisited by Bjerknes and Palmén (1937) and fronts are considered as narrow transition zones characterized by a strong horizontal temperature gradient. This property is often referred to as defining (or "primary") quantity for front detection (Thomas and Schultz, 2019). In addition, dynamical processes occurring along fronts (see Introduction), lead to further characteristic features of fronts – sometimes referred to as "secondary" quantities (Thomas and Schultz, 2019) – such as cyclonic vorticity, strong vertical motion, enhanced stability and a positive potential vorticity (PV) anomaly (e.g. Hoskins, 1982).

Since all these properties are not unique features of fronts (e.g. a strong horizontal temperature gradient can occur along coastlines due to differential heating of land and sea), several of these quantities and their combinations have been utilized for front identification (e.g. Renard and Clarke, 1965; Simmonds et al, 2011; Parfitt et al, 2017), out of which the thermal front parameter (TFP, Sec. 2.3) (Renard and Clarke, 1965) and the F diagnostic (Sec. 2.4) (Parfitt et al, 2017) are the most used. The TFP method is based on a primary quantity only, while the F diagnostic additionally takes a secondary quantity into account. However, both methods do not have a natural basic state, therefore we introduce the dynamic state index (DSI, Sec. 2.5), which is an exact measure of the deviation from a general non-linear wind balance, for front detection. Generally, front detection methods are used to filter out frontal zones and front lines from gridded data. The procedure for this consists of three steps: (1) using one or more meteorological input variables, (2) apply a function to them, and (3) test for a threshold exceedance (Hewson, 1998). At the end, graphical filters can be applied, e.g. to delete disconnected pixels (e.g. Berry et al, 2011; Kern et al, 2019).

## 2.2 The case study: A rapid cyclogenesis, 14.02.2014

In a rapid cyclogenesis, diabatic processes play – in addition to baroclinic instability – a central role for the cyclone intensification (e.g. [Wernli and Gray, 2024](#)). Thereby, mid-tropospheric diabatic heating contributes to a coupling of an upper-level PV anomaly, caused by a dry intrusion of stratospheric air into the troposphere, with a low-level PV anomaly, forming a "PV tower" (e.g. [Hoskins, 1990](#); [Rossa et al, 2000](#)). Here, we use a rapidly intensifying cyclone as a case study which has already been analyzed intensively with a focus on precipitation caused during its life cycle ([Bott, 2016](#)).

[Fig. 1](#) shows a trough west of Ireland at 14.02.2014 12 UTC with a low pressure system on its south-eastern side, which is partly occluded and clearly shows a warm front (over France) and a cold front (west of Portugal). The jet stream flows over the cold front, so that it is cata-type in the northern part and ana-type in the southern part. Along the fronts the specific humidity is particularly high. Maxima of the vertical velocity can be seen in the area of the occlusion and at the back of the ana cold front. This cyclone was part of a series of rapid intensifying cyclones over the North Atlantic in February 2014 ([Volonté et al, 2018](#)).

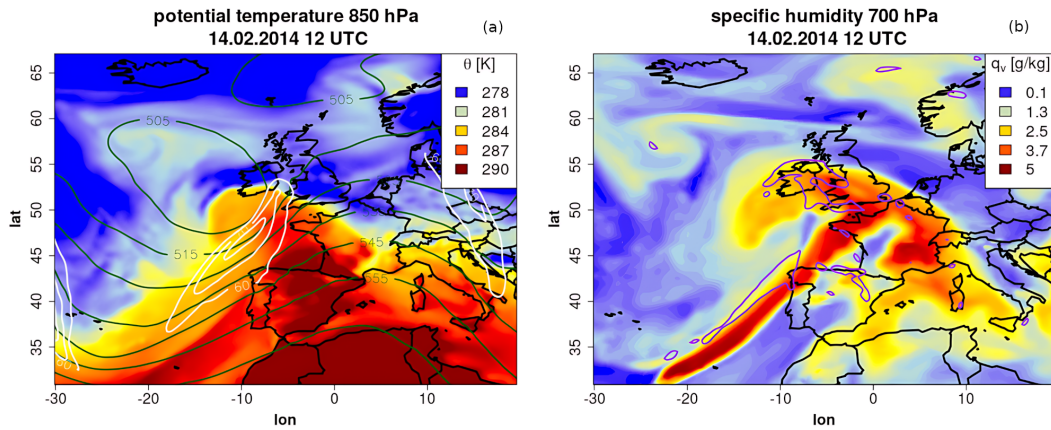


**Fig. 1** Weather situation 14.02.2014 12 UTC. (a) Potential temperature at 850 hPa with contour lines of geopotential height at 500 hPa (darkgreen, in gpdm) and of the horizontal wind at 300 hPa (white, in m/s). (b) Specific humidity at 700 hPa with contour line of -1 Pa/s updraft (purple).

## 2.3 Method 1: Thermic front parameter

Fronts as air mass boundaries are characterized by high baroclinicity, i.e. a pronounced horizontal gradient  $\nabla_h \tau$  in a temperature-based quantity  $\tau$ . To formalize this approach to an automatic detection method, [Renard and Clarke \(1965\)](#) introduced the thermal front parameter (TFP) through

$$TFP(\tau) := -\nabla_h \|\nabla_h \tau\| \cdot \frac{\nabla_h \tau}{\|\nabla_h \tau\|}. \quad (1)$$

The first factor is given by the horizontal gradient of the baroclinicity and thus represents horizontal variations in baroclinicity. The second factor is the horizontal unit vector along the thermal gradient, and through the scalar multiplication of both terms only their parallel projection is considered, such that the TFP is a measure for the horizontal change of baroclinicity along the thermal gradient. For  $\tau$  different thermal quantities can be considered, usually either potential temperature  $\theta$  (e.g. [Berry et al, 2011](#)) or equivalent-potential temperature  $\theta_e$  (e.g. [Schemm et al, 2015](#)). [Thomas and Schultz \(2019\)](#) showed, that using  $\tau = \theta_e$  for front detection leads to artificial fronts in the tropical regions due to high moisture content. To avoid this problem we use  $\tau = \theta$  in accordance with e.g. [Berry et al \(2011\)](#). [Fig. 2](#) shows the TFP at 850 hPa exemplary for the considered case study. The TFP has a dipole structure, with negative values at the front side of the warm front and the occluded front, and positive values at the front side of the cold front. The cold front is not visible in the TFP, so the cold front is detached from the frontal system, which is a characteristic feature of Shapiro-Keyser lows ([Shapiro and Keyser, 1990](#)).

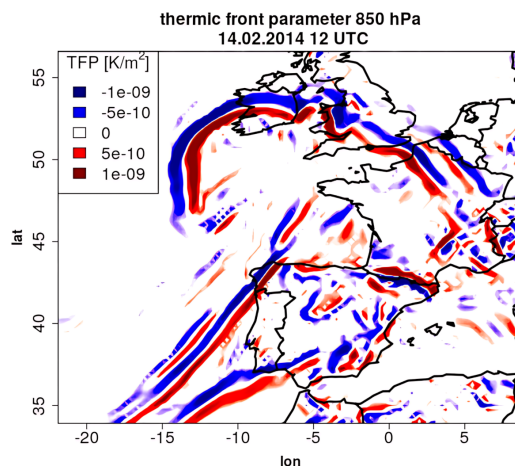


**Fig. 2** Thermic front parameter (TFP) at 850 hPa, 14.02.2014 12 UTC.

Using the TFP concept, [Hewson \(1998\)](#) developed an algorithm that allows the detection of fronts as front lines as well as frontal zones (algorithm 1): First, the location of the front line is determined. In the frontal zone, the norm of the gradient of the thermal quantity  $\tau$  is the largest, so that the first partial derivative has a maximum there. The second spatial derivative has a minimum at the front of the frontal zone (which is called front line) and the third derivative a root, which must be determined (see [Kern et al \(2019\)](#) their Fig. 2 and 3). In order to additionally take into account the curvature of the front, the divergence along the unit vector  $\hat{s}$  is considered resulting in Eq. 2, which was simplified by [Huber-Pock and Kress \(1981\)](#) to Eq. 3. To filter out the front, masking conditions are applied. The first masking condition (Eq. 4) states that the TFP must have a minimum value of  $K_1$ . The value of  $K_1$  depends on the used thermal quantity, the pressure level and the grid size. Here we follow [Kern et al \(2019\)](#)

---

**Algorithm 1:** Front identification using TFP according to [Hewson \(1998\)](#)

---

**front lines**

$$\text{front locator:} \quad \frac{\partial(\|\nabla_h\|\nabla_h\tau\|)}{\partial\hat{s}} = 0 \quad \text{with} \quad \hat{s} = \frac{\nabla_h\|\nabla_h\tau\|}{\|\nabla_h\|\nabla_h\tau\|} \quad (2)$$

$$\nabla TFP(\tau) \cdot \frac{\nabla_h\tau}{\|\nabla_h\tau\|} = 0 \quad (3)$$

$$\text{masking variable 1:} \quad TFP(\tau) > K_1 \quad (4)$$

$$\text{masking variable 2:} \quad S(\tau) := \|\nabla_h\tau\| > K_2 \quad (5)$$

⋮

masking variable n

---

**frontal zones**

$$TFP(\tau) > K_1 \quad (6)$$


---

and use  $K_1 = 0.3 \cdot 10^{-10}$  K/m for 850 hPa level, which is similar to [Hewson \(1998\)](#) and [Parfitt et al \(2017\)](#) ( $K_1 = 0.33 \cdot 10^{-10}$  K/m for 900 hPa) but different from [Catto and Pfahl \(2013\)](#) ( $K_1 = -8 \cdot 10^{-12}$  K/m for the wet-bulb potential temperature at 850 hPa). Fig. 3a shows the front locator (thin red lines), the first masking condition (orange shading) and the intersection of both resulting in the (preliminary) front lines (thick red lines). The occlusion front, warm front, ana cold front and also a part of the cata cold front displaced to the ana cold front are detected. To further filter the front lines, [Hewson \(1998\)](#) used the strength of the front  $S(\tau)$  given by Eq. 5. If the second masking condition is applied (Fig. 3b), then only the part of the (preliminary) front lines from the first masking step are kept which also show a minimum strength. Due to the lower baroclinicity, the warm front and a part of the occlusion front are now not captured, even when using a comparatively small threshold of  $K_2 = 1.35 \cdot 10^{-5}$  K/m ([Hewson, 1998](#); [Parfitt et al, 2017](#); [Kern et al, 2019](#)). Since this is not intentional, we use only the first masking step in this study. This also allows filtering for frontal zones directly (Eq. 6). Consequently, warm fronts are located at the end of the warm air advection and cold fronts at the beginning of the cold air advection.

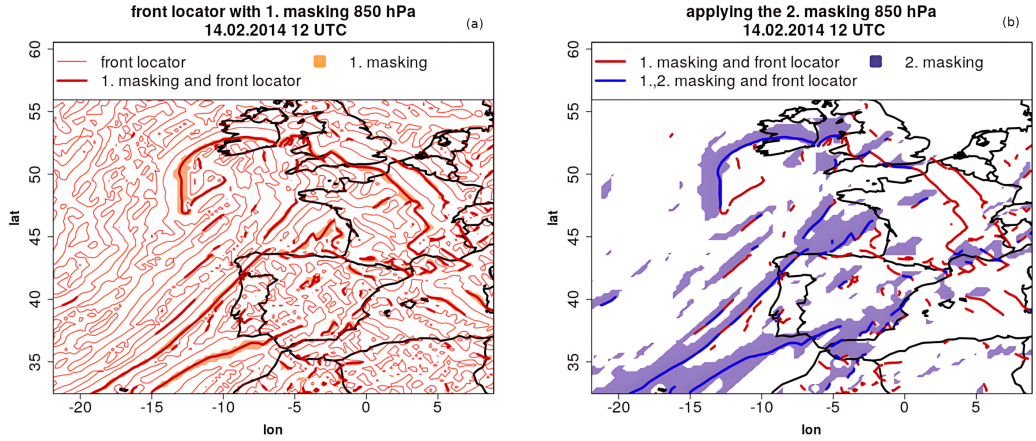


**Fig. 3** Front identification using the TFP method. (a) Front locator (thin red line), the first masking condition (orange shade) and the intersection of both (thick red line). (b) Results from the first masking step (thick red line), the second masking condition (blue shade) and the intersection of both (thick blue line).

## 2.4 Method 2: F diagnostic

Parfitt et al (2017) use the fact that fronts are regions of strong temperature gradients *and* maximal vorticity to develop a new front identification method (algorithm 2), which only allows the detection of frontal zones (and not lines): F is a empirically

---

**Algorithm 2:** Front identification using F diagnostic according to Parfitt et al (2017)

---

$$\text{defining quantity: } F := \frac{\zeta \|\nabla_h T\|}{f \|\nabla_h T\|_0} \quad (7)$$

$$\text{masking: } F \begin{cases} > 1, & \text{for low-level fronts} \\ > 2, & \text{for upper-level fronts (from 600 hPa)} \end{cases} \quad (8)$$


---

determined and dimensionless quantity containing the relative vorticity  $\zeta$  (on isobaric surfaces), the Coriolis parameter  $f$ , the temperature  $T$  and a empirical determined constant  $\|\nabla T\|_0 = 0.45 \text{ K}/(100 \text{ km})$ . The threshold values used for masking (Eq. 8) were also determined empirically based on ERA-Interim (Parfitt et al, 2017).

We point out that F contains the Rossby number

$$Ro := \frac{\zeta}{f} \begin{cases} \ll 1 & \rightarrow \text{synoptic scale} \\ \approx 1 & \rightarrow \text{mesoscale} \\ \gg 1 & \rightarrow \text{convective scale,} \end{cases} \quad (9)$$



which describes the ratio of inertia to Coriolis force and can be interpreted as a measure for the spatial scale. Consequently, by using the  $F$  diagnostic for front detection, fronts are perceived on the basis of their spatial scale weighted with the horizontal temperature gradient. The  $F$  diagnostic (Fig. 4a) shows high values in the low center and along the occlusion front due to high relative vorticity caused by the dry intrusion, which generates potential instability and thus can initiate convection (Browning, 1997). Positive  $F$  values also occur along the ana cold front and at a small part of the warm front, while negative  $F$  values are inevitably connected to negative relative vorticity. If now the masking condition  $F > 1$  is applied, the frontal zones shown in Fig. 4b result. Thereby, the low center is erroneously detected as a front and the warm and cold fronts are detected only to a small part detached from the low center. Since baroclinicity and relative vorticity are not independent of each other but are positively correlated (Hoskins, 1982), only particularly strong fronts are detected with the  $F$  diagnostic, while weaker fronts remain unrecognized.

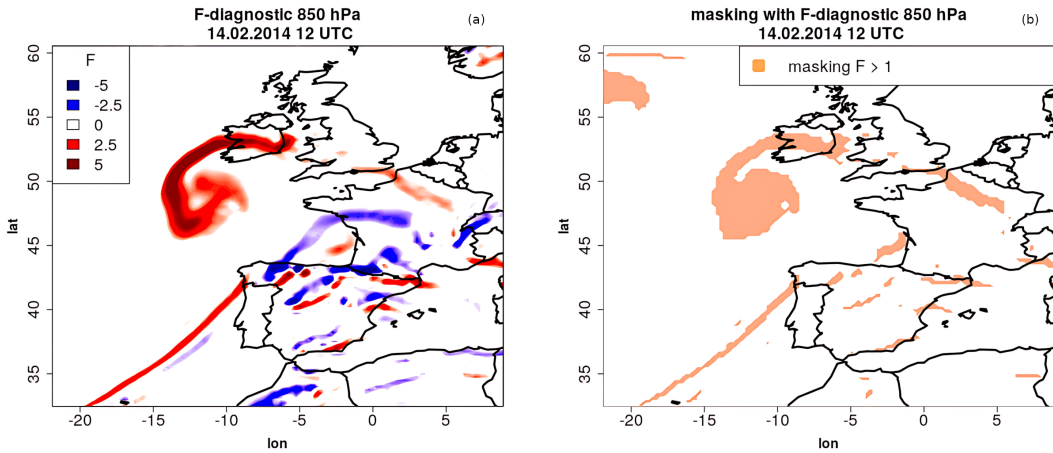


**Fig. 4** Front identification using the  $F$  diagnostic. (a)  $F$  diagnostic at 850 hPa. (b) Masking condition  $F > 1$ .

## 2.5 Method 3: Dynamic State Index (DSI)

In this section the concept of the dynamic state index (DSI) is introduced based on the derivation of a general non-linear solution of the primitive equations, called steady wind. Using the case study from before the DSI structure of the fronts is showcased, which is then used to develop a new algorithm for front identification by applying the DSI as masking variable.

### 2.5.1 The concept of the dynamic state index (DSI)

In order to investigate flows systematically, they are often divided into a basic state and a deviation from it. This basic state can, for example, be determined statistically with the mean value. The deviation is then given in first order by the standard

deviation. Such a statistical approach has the disadvantage that the mean value does not necessarily represent a solution of the basic equation system and is therefore not balanced. For this reason, a dynamic basic state is desirable which itself represents a solution to the primitive equations. Here, we consider an adiabatic and stationary basic state leading to the steady wind solution of the primitive equations (Schär, 1993) and the deviations from it are given by the DSI (Névir, 2004; Weber and Névir, 2008). The advantage of this "dynamical" approach is that the basic state is balanced, however, it has to be derived first. The derivation procedure is summarized in Fig. 5 and detailed in the following.

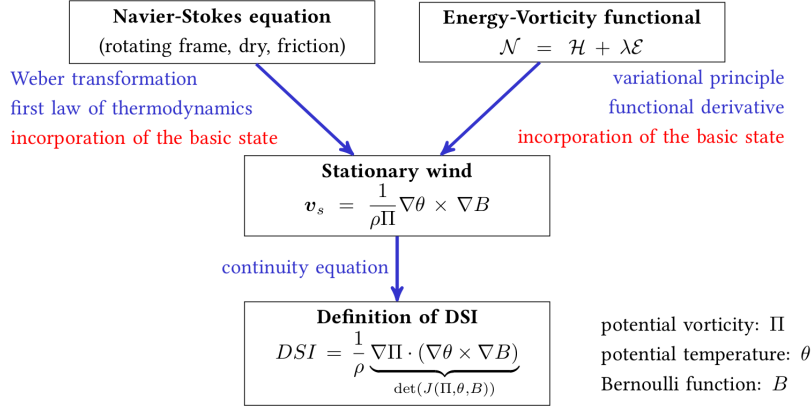


**Fig. 5** Scheme that shows the different ways to derive the DSI. The two left arrows (i.e., derivation of steady wind from Navier-Stokes equation, and derivation of DSI from inserting the steady wind in the continuity equation) were detailed in the text.

### 2.5.2 The steady wind representation and its interpretation

The derivation of the steady wind starts directly from the primitive equations (all steps are detailed in appendix A). The first law of thermodynamics is incorporated into the Navier-Stokes equation leading to an alternative version, that combines momentum and energy conservation in one equation. Then the basic state (adiabatic, steady, inviscid) is incorporated, which means that diabatic, instationary and friction terms are omitted. This yields an expression for the convective flux of the PV (Schär, 1993)  $\rho\Pi\mathbf{v} = \nabla\theta \times \nabla B$ , which can be rearranged to

$$\mathbf{v}_s = \frac{1}{\rho\Pi} \nabla\theta \times \nabla B, \quad (10)$$

what is called the steady wind representation by Schär (1993) and Névir (2004). It contains four constituting quantities: the air density  $\rho$ , the potential temperature  $\theta$ , the Bernoulli function  $B := \Phi + 0.5\mathbf{v}^2 + h$ , which represents the most general stream function as the sum of potential energy  $\Phi$ , kinetic energy  $0.5\mathbf{v}^2$  (based on the wind

	geostrophic wind	pseudo-geostrophic wind	steady wind
formula	$\mathbf{v}_{g,h} = \frac{1}{f} \mathbf{k} \times \nabla_h \Phi$	$\mathbf{v}_{pg,h} = \frac{1}{\zeta + f} \mathbf{k} \times \nabla_h \left( \frac{1}{2} \mathbf{v}_h^2 + \Phi \right)$	$\mathbf{v}_s = \frac{1}{\rho \Pi} \nabla \theta \times \nabla B$
vortical quantity	$f$	$\zeta + f$	$\rho \Pi$
energetic quantity	$\Phi$	$\frac{1}{2} \mathbf{v}_h^2 + \Phi$	$B$
dimensions	2	2	3

**Table 1** Different common wind approximations (geostrophic wind, pseudo-geostrophic wind and steady wind) and the contributing energetic and vortical quantities compared. The complexity increases from left to right with the steady wind as most general wind representation.

vector  $\mathbf{v} = (u, v, w)^T$ ) and enthalpy  $h$ . The potential vorticity  $\Pi := \rho^{-1} \boldsymbol{\xi}_a \cdot \nabla \theta$  (utilizing the absolute vorticity  $\boldsymbol{\xi}_a$ ) describes the circulation on isentropic surfaces and is a central quantity in atmospheric vorticity dynamics (Ertel, 1942; Hoskins et al, 1985). Under adiabatic and stationary conditions,  $\mathbf{v}_s$  does not intersect the tubes spanned by  $\nabla B$  and  $\nabla \Pi$  and therefore, does neither constitute to the PV tendency nor to energy conversions, which is why Gaßmann (2014, 2019) refers to it as "inactive" wind. The real wind can be decomposed by  $\mathbf{v} = \mathbf{v}_s + \mathbf{v}_a$  into steady (inactive) wind and the deviation from it, the so-called active wind  $\mathbf{v}_a$  (Gaßmann, 2014). Compared to the geostrophic wind decomposition, the active wind can be seen as analogy to the ageostrophic wind. The vertical component of the steady wind  $w_s$  describes isentropic upglide, while the deviation from it  $w - w_s$  behaves similarly to the isentropic displacement wind (Hoskins et al, 2003; Gaßmann, 2019), which affects baroclinicity by tilting of isentropic surfaces (Papritz and Spengler, 2015).

A comparison of the steady wind  $\mathbf{v}_s$  with other wind representations reveals a hierarchy in terms of the contributing energetic and vortical quantities (Tab. 2.5.2). The geostrophic wind  $\mathbf{v}_{g,h}$  contains as energetic quantity the potential energy  $\Phi$ , which acts as stream function, and as vortical quantity the Coriolis parameter  $f$ , which represents the external rotation only. The pseudo-geostrophic wind  $\mathbf{v}_{pg,h}$  (derived under the assumption  $\partial \mathbf{v}_h / \partial t = 0$ ) contains the sum of potential and kinetic energy as energetic quantity and the absolute vorticity  $\zeta + f$ , i.e. external and internal rotation, as vortical quantity (Lange, 2002). The kinetic energy (following from considering the advection term) introduces non-linearity, while the geostrophic wind solution is linear. The steady wind  $\mathbf{v}_s$  additionally includes thermodynamic information, such that the energetic quantity is the Bernoulli function and the vortical is the "PV substance"  $\rho \Pi$ .  $\mathbf{v}_s$  is thus the most general wind representation, which contains all external and internal energetic and vortical aspects (Schär, 1993; Lange, 2002; Névir, 2004).

The fact that all the wind representations contain an energetic and a vortical quantity shows that the two are equally important conserved quantities and represent constraints to the flow, which reduce the phase space dynamics. Based on this observation, a generalized theory can be derived – the energy-vorticity theory (EVT) – which unifies the separate ways of thinking of a pure energy-based theory (Hamilton mechanics) and a pure vorticity theory (PV thinking) into a common theory based on Nambu mechanics (Névir and Blender, 1993; Névir and Sommer, 2009). In the EVT framework the steady wind can also be derived by minimizing the energy-vorticity functional containing total energy and potential enstrophy (e.g. Weber and Névir, 2008).

### 2.5.3 The Dynamic State Index (DSI)

For the derivation of the DSI (summarized in Fig. 5), we insert  $\mathbf{v}_s$  in the continuity equation  $\nabla \cdot (\rho \mathbf{v}_s) = 0$ , yielding  $\nabla \Pi \cdot (\nabla \theta \times \nabla B) = 0$ . This motivates the definition of the dynamic state index DSI (Névir, 2004) by

$$DSI := \frac{1}{\rho} (\nabla \theta \times \nabla B) \cdot \nabla \Pi = \frac{1}{\rho} \det \left( \frac{\partial(\theta, B, \Pi)}{\partial(x, y, z)} \right) \quad (\text{determinant form}). \quad (11)$$

In the second equality the triple product is reformulated in terms of the determinant of the Jacobian. The DSI combines the Lagrangian conserved quantities  $\theta$  and  $\Pi$  with the most general stream function  $B$  and measures their phase space volume. In this sense, it can be seen as a generalization of the PV- $\theta$  view on atmospheric circulation (Hoskins, 1991).

By applying the product rule the DSI can equivalently be written as

$$DSI = -\frac{\Pi^2}{\rho} \nabla \cdot (\rho \mathbf{v}) \quad (\text{divergence form}) \quad (12)$$

$$= \mathbf{v} \cdot \nabla \left( \frac{\Pi^2}{2} \right) \quad (\text{advection form}). \quad (13)$$

The divergence form describes the continuity of the stationary wind and the advection form the advection of the squared PV, which can be considered as mass specific potential enstrophy. In the basic state with  $\mathbf{v} = \mathbf{v}_s$ , the divergence  $\nabla \cdot \mathbf{v}_s$  and the advection of potential enstrophy vanish, such that  $DSI = 0$ . Furthermore, the advection of  $\nabla \theta, \nabla B$  and  $\nabla \Pi$  disappear in the basic state. At the same time, PV is a function of  $B$  in the basic state, leading to a coupling of energetic and vortical quantity and thus a reduced non-linearity. This coupling between PV and B is a prerequisite in the PV thinking, but a dynamical evolution of the system is only possible if PV and B are independent from each other, that is, exactly when  $DSI \neq 0$  (Lange, 2002). Overall, the DSI values can precisely be interpreted by

$$DSI \begin{cases} = 0, & \text{stationary, adiabatic, reversible and frictionless flow (i.e. basic state)} \\ \neq 0, & \text{non-steady, diabatic or viscous flow.} \end{cases} \quad (14)$$

### 2.5.4 Using the DSI for front identification

Fig. 6 shows the PV together with the horizontal wind and the DSI for the considered case study. The PV is maximal in the frontal regions due to large cyclonic vorticity, a large horizontal temperature gradient and strong stability. The PV anomalies along fronts arise from diabatic heating, e.g., due to condensation in the warm conveyor belt, evaporation of precipitation in the dry intrusion, convection, turbulent mixing and longwave radiative effects, as in detail studied based on PV tendencies by Chagnon et al (2013) and Attinger et al (2021). The DSI shows a dipole structure along the fronts with negative values downstream and positive values upstream,

reflecting an oscillation around the basic state, i.e. the energy-vorticity equilibrium. To explain this structure, the advection form of the DSI (Eq. 13) is considered. Based on the wind decomposition in steady (inactive) and active wind through  $\mathbf{v} = \mathbf{v}_s + \mathbf{v}_a$ , Gaßmann (2014) showed that in the horizontal (index  $h$ ) the stationary wind dominates the active wind (i.e.,  $\mathbf{v}_{s,h} \gg \mathbf{v}_{a,h}$ ) and thus can be used as approximation for the real wind (i.e.,  $\mathbf{v}_h \approx \mathbf{v}_{s,h}$ ). Consequently, a zonal wind crossing a cyclonic PV anomaly leads to positive values upstream (due to  $\nabla\Pi^2 > 0$ ) and negative values downstream (due to  $\nabla\Pi^2 < 0$ ). Thus, frontal zones are characterized by large  $|DSI|$  values. From inserting the wind decomposition into the continuity equation (Gaßmann (2014), therein Eq. 2.24), it can further be concluded, that positive (normalized) DSI values depict a source for the active wind, while negative values depict a sink for the active wind (Gaßmann, 2014, 2019). The vertical active wind (and the in shape similar isentropic displacement wind) pushes the isentropic surfaces down ahead of a front, leading to adiabatic warming (in the warm sector), while at the backside of the front the isentropes are pushed up, associated with adiabatic cooling (in the cold sector) (Hoskins et al, 2003). The horizontal active wind generates kinetic energy, when it points towards low pressure (Gaßmann, 2019) and can thus be seen as analogy to the ageostrophic wind, which contains the isallobaric wind (that "blows" perpendicular to lines of the same pressure fall tendency). From the simplification of viewing fronts as discontinuity surfaces it can be deduced, that fronts always move to the area of the greatest pressure fall tendency, which corresponds to the front-perpendicular component of the isallobaric wind (Zdunkowski and Bott, 2003). In this way, the DSI can be used as a diagnostic indicating dynamically active regions, in analogy to the divergence of the  $\mathbf{Q}$  vector, which – derived from the quasi-geostrophic 'omega'-equation – indicates vertical motions and is thus used as an indicator of frontogenesis (Hoskins et al, 1978; Steinacker, 1999).

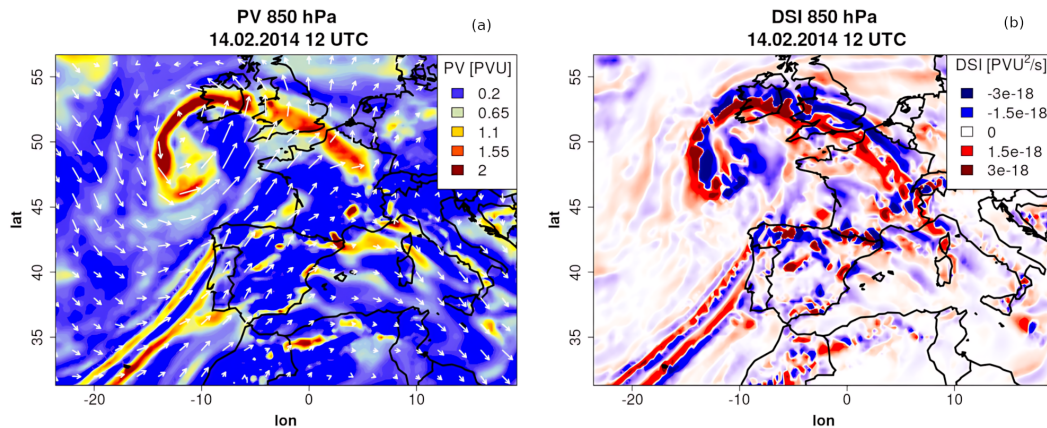


**Fig. 6** (a) Potential vorticity (coloured) and horizontal wind (white arrows) both at 850 hPa. (b) DSI at 850 hPa.

In addition to these theoretical considerations, data-based studies can help to better understand the behaviour of the DSI. Müller et al (2018) showed that the structure of frontal rain bands is reflected in the DSI, and based on time series analysis, Claussnitzer and Névir (2009) and Claussnitzer (2010) demonstrated that  $|DSI|$  shows a high correlation with precipitation sums. Moreover, von Lindheim et al (2021) showed that the DSI is associated with persistent and coherent structures in atmospheric flows, like fronts. All these properties make the DSI a suitable tool to identify fronts as deviation from the adiabatic and steady basic state. For this purpose, we have developed the following algorithm (algorithm 3):

---

**Algorithm 3:** Front identification using DSI ("DSI method")

---

**front lines**

$$\text{front locator: } \|\nabla_h DSI\| \cdot \frac{\nabla_h \Pi}{\|\nabla_h \Pi\|} = 0 \quad (15)$$

$$\text{masking: } DSI < q_{p_1}(DSI) \quad (16)$$


---

**frontal zones**

$$\text{masking: } |DSI| > q_{p_2}(DSI) \quad (17)$$


---

For the front locator, we consider the gradient of the DSI projected onto the unit vector of the PV. This is inspired by the TFP method (Eq. 3), but in contrast to the unit vector of the thermic quantity we use the unit vector of the PV, which always points in the direction of the frontal zone and consequently allows us to outline the whole frontal zone (front and back side). In order to filter out just the front line, the DSI must have particularly negative values, which can be measured by using a small percentile  $q_{p_1}$  (masking Eq. 16). As Fig. 7 shows, the occlusion front, the warm front and the ana cold front are detected in the case study. Compared to the TFP method, the cold front line is more interrupted, and in contrast to the F diagnostic, the entire warm front is detected.

Frontal zones are detected by particularly high values of the magnitude of the DSI (Eq. 17), by using a large percentile  $q_{p_2}$ . This is different from the TFP method, where only the positive values (and not the absolute values) are used to capture frontal zones. We determine the threshold values using an area over the North Atlantic (see Fig. 8) that is undisturbed by orography. The percentiles are calculated for every pressure level separately to account for the average increase in DSI with height. Using a percentile allows to adjust the sensitivity of our method and to adapt it to the model resolution, since higher resolved models tend to have higher DSI values (Weijenborg et al, 2015).

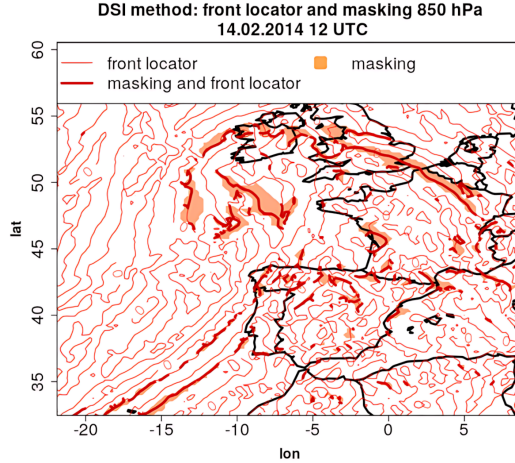


**Fig. 7** DSI method: Front locator (thin red lines), masking condition (orange shading) and the intersection of both (thick red lines) at 850 hPa, 14.02.2014 12 UTC.

### 3 Results

In this section, we compare the three methods for front identification (TFP, F diagnostic and DSI) spatially and temporally. As the F diagnostic only allows the detection of frontal zones, we consider them only and refer to them as "fronts" for the sake of simplicity. In the end, we examine the essential characteristics of the respective detected fronts. For this purpose, we consider mid-level fronts at 600 hPa. Using 850 hPa (as shown before) is unfavorable not only due to strong orography influence but also due to the influence of the boundary layer, which itself is strongly influenced by the land-sea contrast and the sea surface temperature (e.g. [Parfitt et al, 2016](#)).

#### 3.1 Climatology

Fig. 8 shows the occurrence probability of detected fronts (global north winter climatology, i.e. DJF 2000-2019, based on hourly ERA5 data) using the three previously described methods. The TFP method detects the Northern Hemisphere Atlantic and Pacific storm tracks, which are partly washed out to the north. The Southern Hemisphere (summer) storm tracks are also recognizable in lower intensity. The F diagnostic (using the recommended threshold  $F > 2$  for mid-level fronts) shows strong signals along the Northern Hemisphere storm tracks, but only weak signals along the Southern Hemisphere storm tracks. The region around the equator is masked out due to the convergence of the Coriolis parameter, as recommended by [Parfitt et al \(2017\)](#). The DSI method detects clearly the Northern Hemisphere storm tracks with their typical characteristics – northward tilt and eastward intensity decrease ([Hoskins and Hodges, 2002](#)). The Southern Hemisphere storm tracks are detected by the DSI method as well, and in a stronger intensity than with the F diagnostic. Compared to the TFP method, the Southern Hemisphere storm tracks detected by the DSI method are more

pronounced over the Atlantic and Indian Ocean, which is consistent with the cyclogenesis density found by [Hoskins and Hodges \(2005\)](#). All methods show also signals along the inner tropical convergence zone.

### 3.2 Annual cycle

In order to quantitatively compare the annual variation of the determined number of fronts with the three methods and to avoid bias due to orography, only a box (shown in Fig. 8) over the North Atlantic is used. Fig. 9 shows the annual cycle of the detected fronts at 600 hPa over this North Atlantic box with the TFP method, the F diagnostic and the DSI method for the three percentiles 95 %, 97 %, and 99 %, respectively. Here, ten years from 2010 to 2019 (each day 0 UTC) were considered. All methods detect more fronts in winter than summer, which can be explained by the northward shift of the storm tracks, while the considered box remains fixed, and, regardless of the area considered, baroclinicity, mean wind speed and thus relative vorticity are on average weaker in summer than in winter (e.g. [Hoskins and Hodges, 2002](#)). With the TFP method, fewer fronts are detected each month than with the F diagnostic, which is in agreement with the global climatology previously considered. The range between the minimum and maximum monthly front number is greater with the F diagnostic than with all other methods, which can be explained by the fact that both baroclinicity and relative vorticity are higher on average in winter than in summer, and using their product in the F diagnostic then overemphasizes this difference. The DSI method also reflects the annual cycle for all percentile thresholds, although the summer-winter spread is not as pronounced with the DSI method, especially when the threshold is increased. The fact that more fronts are recorded with the DSI method in summer than with the other methods is possibly due to the construction of the DSI. Regardless of the amount of baroclinicity itself, fronts represent a deviation from the basic state in every season. In addition, the availability of moisture for diabatic processes is larger in summer due to higher temperatures, which correlates with  $|DSI|$  ([Claussnitzer et al, 2008](#); [Claussnitzer and Névir, 2009](#)).



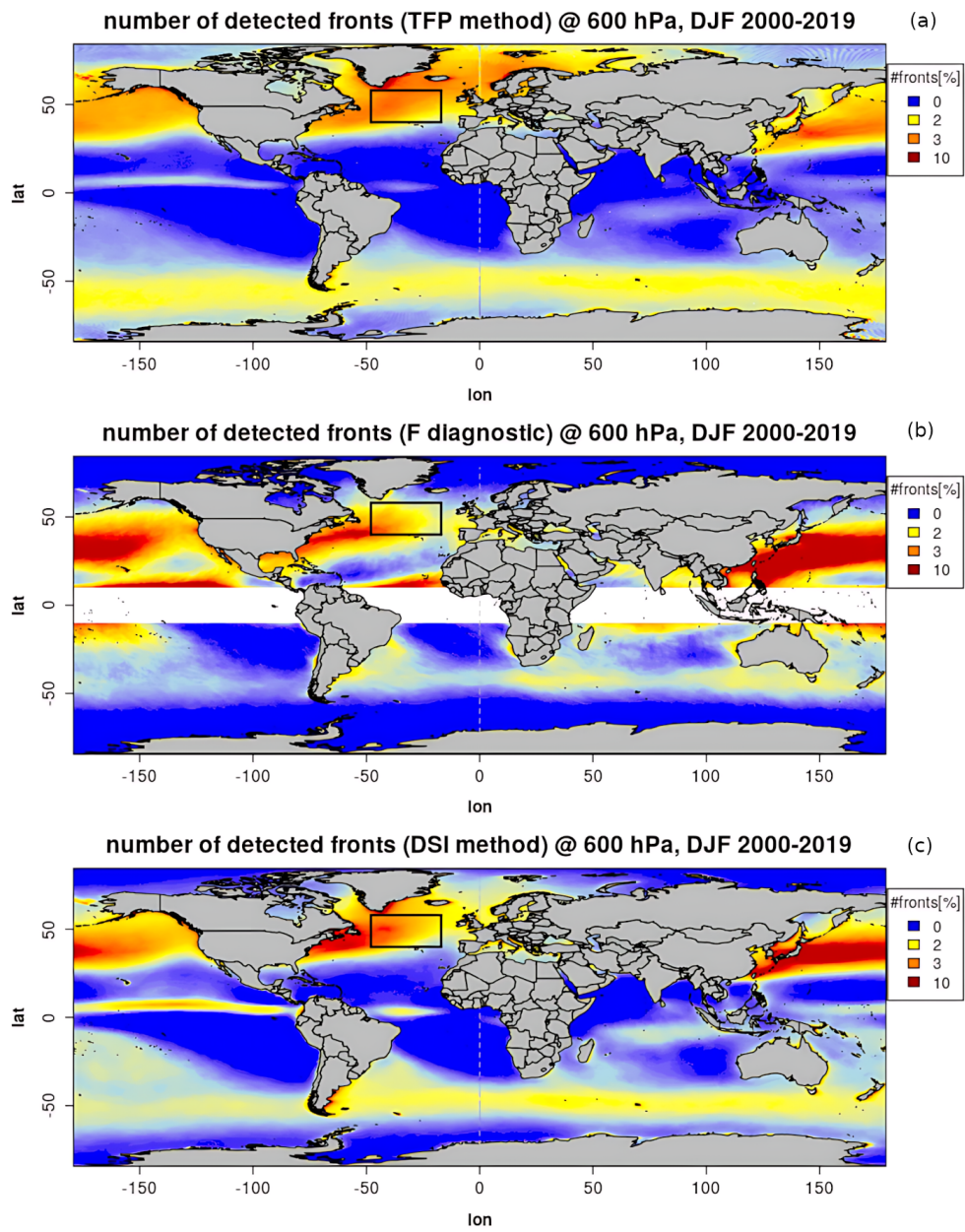


**Fig. 8** Front Climatology: Number of detected fronts (measured as occurrence probability) for twenty north winters (DJF 2000-2019) using (a) TFP method, (b) F diagnostic and (c) DSI method with 95 % percentile.

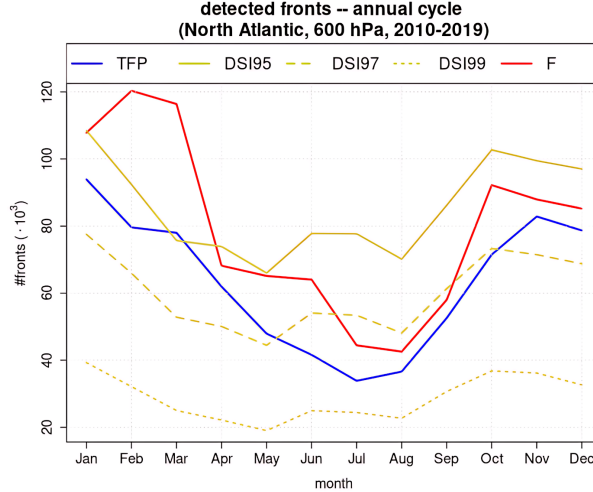


**Fig. 9** Annual cycle of detected fronts: Average number of detected fronts per month using TFP method, F diagnostic and DSI method (percentiles 95 %, 97 % and 99 %, respectively) at 600 hPa over the North Atlantic between 2010-2019.

### 3.3 Properties of the detected fronts

In this section, the properties of the detected fronts are compared. Fig. 10 shows the distribution of specific humidity, baroclinicity measured by  $\|\nabla_h T\|$  and relative vorticity of the fronts detected with the TFP method, the F diagnostic and the DSI method (95 % percentile), respectively. Fronts detected with the TFP method show high baroclinicity (due to the definition of the TFP) and anticyclonic vorticity on average. The latter is not reasonable as fronts are associated with lows and itself are areas of high relative vorticity. Fronts detected with the F diagnostic are characterized by high baroclinicity and high relative vorticity (both due to the definition of F) but low specific humidity. This indicates that the constituting variables in the front detection method also dominate the characteristics of the detected fronts. Fronts detected with the DSI method are characterized by high specific humidity and less baroclinicity. Generally, the  $|DSI|$  values correlate with specific humidity, even if the specific humidity is not considered in the (dry) DSI (Claussnitzer et al, 2008). Hittmeir et al (2021) confirmed this theoretically by deriving a hierarchy of DSI variants by step-wise including water vapor ( $q_v$ ) and liquid water content ( $q_c$ ) and the associated phase changes into the basic state of the DSI, which results in additional terms in Eq. 11-13 that contain the respective gradients  $\nabla q_v$  and  $\nabla q_c$ . This emphasizes that the specific humidity is a crucial component of the diabatic processes that cause deviations from a dry basic state. The fact that fronts detected using the DSI method have less baroclinicity than fronts determined using the other methods, which contain baroclinicity directly as a factor, can be seen from the determinant form of the DSI (Eq. 11): Of the six contributing terms, only four contain horizontal derivatives of potential temperature, while the static stability in the other two terms is scaled with the horizontal gradients of  $\Pi$ ,  $B$  that are larger than their vertical ones. Hence, the DSI reflects not

only individual selected properties of fronts but their versatility, and the relative contribution of baroclinicity is thus smaller. Altogether, the DSI can be interpreted as an *activation parameter*, indicating regions where energy is released, while baroclinicity is an *availability parameter* describing a development potential (e.g. Schartner et al, 2009).

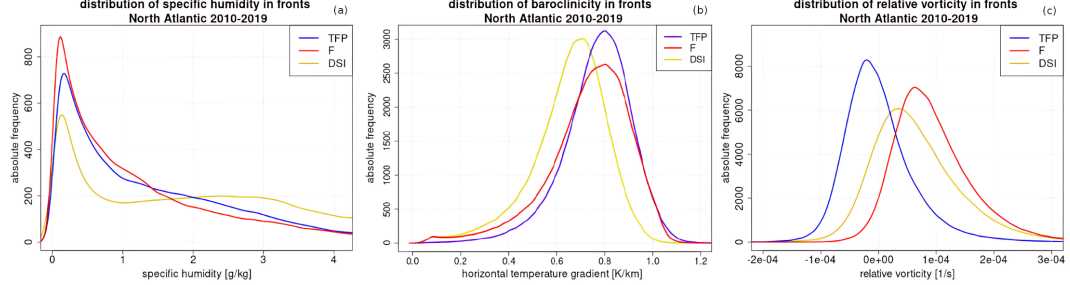


**Fig. 10** Front properties: Distribution of (a) specific humidity, (b) baroclinicity and (c) relative vorticity in the respective detected fronts (TFP method, F diagnostic, DSI method with 95 % percentile) at 600 hPa over the North Atlantic between 2010-2019.

Following Hewson (1998), the movement speed of front lines, determined as contours of a quantity  $\Psi$ , can be estimated by

$$v_f = \mathbf{v}_h \cdot \frac{\nabla_h \Psi}{\|\nabla_h \Psi\|} = \mathbf{v}_h \cdot \mathbf{e}_\Psi \leq \|\mathbf{v}_h\|. \quad (18)$$

The horizontal wind  $\mathbf{v}_h$  is projected onto the horizontal unit vector  $\mathbf{e}_\Psi$ , so that the maximum front speed is constrained by  $\|\mathbf{v}_h\|$ . Since Eq. 18 considers the displacement of contours (and not surfaces), the front speed is calculated only for the TFP method ( $\Psi = TFP$ ) and the DSI method ( $\Psi = DSI$ ). The average front speed in the North Atlantic box using the TFP method is 12,6 m/s in winter and 9,5 m/s in summer, while using the DSI method it is 17,1 m/s in winter and 13,8 m/s in summer (both normalized with the respective number of fronts detected). Since the selected quantity  $\Psi$  enters the calculation of the speed of movement only via the unit vector (i.e. as a direction and not as magnitude), it can be deduced that  $\mathbf{e}_{DSI}$  is on average "more parallel" to  $\mathbf{v}_h$  than  $\mathbf{e}_{TFP}$ . This confirms the capacity of the DSI to indicate the direction of movement (see, Fig. 6).

## 4 Summary and discussion

We discuss various methods for identifying fronts from reanalyses and present a new front detection method based on the dynamic state index (DSI), which accurately measures the deviation from an adiabatic, steady and inviscid basic state that represents a general non-linear solution of the primitive equations.

The discussed methods and the constituting variables are summarized in Tab. 2. The

method	quantities	frontal zones	frontal lines	properties of detected fronts
TFP	$\theta$	yes	yes	baroclinicity
F	$T, \zeta$	yes	no	baroclinicity, vorticity
DSI	$\theta, B, \Pi$	yes	yes	specific humidity

**Table 2** Characteristics of the compared front identification methods: Constituting quantities, features of the methods and properties of the respective detected fronts.

standard method for front detection, which uses the TFP as purely thermal quantity, was extended by Parfitt et al (2017) by including relative vorticity to account for the dynamical processes occurring at fronts. We point out that the F diagnostic contains the Rossby number, and thus detects fronts based on their spatial scale weighted with baroclinicity. By using the DSI, we present an alternative view on front detection by introducing a front detection algorithm that considers fronts as deviation from an adiabatic, steady and inviscid basic state. The DSI has as constituting variables potential temperature, Bernoulli function and potential vorticity and shows a dipole structure along fronts. We show that this DSI method captures the global storm track regions and reflects the annual cycle in front (and cyclone) frequency.

A comparison of the three methods reveals that the F diagnostic detects more fronts in winter than the TFP and DSI method. Further, the spread between summer and winter is largest in the F diagnostic, which can be explained by its construction as multiplication of baroclinicity and relative vorticity, which are positively correlated due to the transverse circulation at fronts (Hoskins, 1982). The DSI methods shows the smallest summer-winter spread in the number of fronts, which can be traced back to the fact that fronts represent a deviation from the basic state regardless of the season. By comparing the properties of the detected fronts, we find that fronts identified using the TFP method are characterized by high baroclinicity but on average anti-cyclonic relative vorticity. Fronts identified with the F diagnostic are characterized by high baroclinicity and high relative vorticity, while fronts identified with the DSI method show particularly high specific humidity. This emphasizes the role of specific humidity in diabatic processes which represent a deviation from a dry and reversible basic state.

Overall, the results indicate that the properties of the detected fronts strongly depend on the method used and in particular the constituting variables, which is consistent with previous findings (Hope et al, 2014; Schemm et al, 2015; Spensberger and Sprenger, 2018; Soster and Parfitt, 2022). This indicates that the front detection method should be chosen with great care and derived properties should be tested for robustness with respect to the method used. Our newly introduced DSI method can hereby provide a more general view on front detection, due to its theoretical foundation and the versatile contributing quantities and processes. The correlation of the DSI with specific humidity and precipitation sums also enables to recognize fronts based on their direct weather impact and could be particularly suitable for investigating extreme precipitation events.

**Acknowledgements.** This research has been supported by Deutsche Forschungsgemeinschaft (DFG) through grant CRC 1114 "Scaling Cascades in Complex Systems",

Project Number 235221301, Project A01 "Coupling a multiscale stochastic precipitation model to large scale atmospheric flow dynamics". ECMWF is acknowledged for providing the ERA5 reanalysis data. The R open-source software package (R Core Team, 2020) has been used to produce the analyses and graphics for this study.

**Data Availability.** The used ERA5 reanalysis data is available at Copernicus Data Store (<https://cds.climate.copernicus.eu/#!/home>).

**Code Availability.** The code has been made available in form of the R Package "meteoEVT" (Mack, 2022) (<https://CRAN.R-project.org/package=meteoEVT>).

## Declarations

**Conflict Interest.** The authors have no relevant financial or non-financial interests to disclose.

## A Derivation of the steady wind representation

The starting point for deriving the DSI is the derivation of a general non-linear solution of the primitive equations by incorporating the basic state, i.e. stationary, inviscid and adiabatic conditions. The Navier-Stokes equation on a rotating Earth with friction under dry conditions is given by

$$\frac{d\mathbf{v}}{dt} + 2\boldsymbol{\omega} \times \mathbf{v} = -\frac{1}{\rho}\nabla p - \nabla\Phi + \mathbf{F}_R, \quad (19)$$

where  $\mathbf{v} = (u, v, w)^T$  represents the 3D velocity field,  $\boldsymbol{\omega}$  the Earth's rotation vector,  $\rho$  the air density,  $p$  the pressure,  $\Phi$  the gravity potential, and  $\mathbf{F}_R$  non-conservative frictional forces. The total derivative of the velocity is decomposed into a stationary and advective part by using the Euler decomposition. The advective part can in turn be decomposed into a vortical and an energetic part with the Weber transformation

$$\frac{d\mathbf{v}}{dt} = \frac{\partial\mathbf{v}}{\partial t} + \mathbf{v} \cdot \nabla\mathbf{v} = \frac{\partial\mathbf{v}}{\partial t} + \nabla\frac{1}{2}\mathbf{v}^2 + \boldsymbol{\xi} \times \mathbf{v}. \quad (20)$$

Using the first law of thermodynamics in the operator form  $dh = Tds + \nu dp$  (with  $h$  the specific enthalpy,  $s$  the specific entropy and  $\nu := \rho^{-1}$ ) and switching the operator  $d$  to  $\nabla$ , an alternative form of the Navier-Stokes equations (constraint by energy conservation) can be derived

$$\frac{\partial\mathbf{v}}{\partial t} + \underbrace{(\boldsymbol{\xi} + 2\boldsymbol{\omega})}_{=: \boldsymbol{\xi}_a} \times \mathbf{v} = T\nabla s - \nabla \underbrace{\left(\Phi + \frac{1}{2}\mathbf{v}^2 + h\right)}_{=: B} + \mathbf{F}_R. \quad (21)$$

The bracketed part is called Bernoulli function  $B$  and describes the most general stream function. Multiplying both sides of the equation with  $\times\nabla\theta$  (where  $\theta$  represents

the potential temperature) and using the definition of the potential vorticity  $\Pi$  leads to

$$\rho\Pi\mathbf{v} - \xi_a \frac{d\theta}{dt} + \xi_a \frac{\partial\theta}{\partial t} - \mathbf{F}_R \times \nabla\theta = - \left( \frac{\partial\mathbf{v}}{\partial t} + \nabla B \right) \times \nabla\theta. \quad (22)$$

At this point, the basic state is incorporated so that the colored terms are omitted, because the flow in the basic state is **stationary**, **adiabatic** and **frictionless**. This yields an expression for the convective flux of the PV (Schär, 1993)

$$\rho\Pi\mathbf{v} = \nabla\theta \times \nabla B. \quad (23)$$

For non-vanishing PV, this equation can be rearranged to

$$\mathbf{v}_s = \frac{1}{\rho\Pi} \nabla\theta \times \nabla B, \quad (24)$$

what is called the steady-state wind representation by Schär (1993) and N evir (2004).

## References

- Attinger R, Spreitzer E, Boettcher M, et al (2021) Systematic assessment of the diabatic processes that modify low-level potential vorticity in extratropical cyclones. *Weather Clim Dynam* 2:1073–1091. <https://doi.org/10.5194/wcd-2-1073-2021>
- Berry G, Reeder MJ, Jakob C (2011) A global climatology of atmospheric fronts. *Geophys Res Lett* 38(L04809). <https://doi.org/10.1029/2010GL046451>
- Bjerknes J (1919) On the structure of moving cyclones. *Geofys Publ* 1(2):1–8
- Bjerknes J, Palm en E (1937) Investigations of selected European cyclones by means of serial ascent. Case 4: February 15-17, 1935. *Geofys Publ* 12(2):1–62
- Bjerknes J, Solberg H (1922) Life cycle of cyclones and the polar front theory of atmospheric circulation. *Geofys Publ* 3(1):3–18
- Bochenek B, Ustrnul Z, Wypych A, et al (2021) Machine Learning-Based Front Detection in Central Europe. *Atmosphere* 12(1312):113–137. <https://doi.org/10.3390/atmos12101312>
- Bott A (2016) *Synoptische Meteorologie: Methoden der Wetteranalyse und -prognose*. Springer Spektrum Verlag, Berlin, Heidelberg, <https://doi.org/10.1007/978-3-642-25122-1>
- Browning KA (1997) The dry intrusion perspective of extra-tropical cyclone development. *Meteorol Appl* 4:317–324
- Catto JL, Pfahl S (2013) The importance of fronts for extreme precipitation. *J Geophys Res Atmos* 118:10791–10801. <https://doi.org/10.1002/jgrd.50852>

- Catto JL, Jakob CL, Berry G, et al (2012) Relating global precipitation to atmospheric fronts. *Geophys Res Lett* 39(L10805). <https://doi.org/10.1029/2012GL051736>
- Catto JL, Nicholls N, Jakob C, et al (2014) Atmospheric fronts in current and future climates. *Geophys Res Lett* 41:7642–7650. <https://doi.org/10.1002/2014GL061943>
- Chagnon JM, Gray SL, Methven J (2013) Diabatic processes modifying potential vorticity in a North Atlantic cyclone. *Q J R Meteorol Soc* 139:1270–1282. <https://doi.org/10.1002/qj.2037>
- Charney J (1947) The dynamics of long waves in a baroclinic westerly current. *J Meteorol* 4:135–162
- Clark PA, Gray SL (2018) Sting jets in extratropical cyclones: a review. *Q J R Meteorol Soc* 144:943–969
- Claussnitzer A (2010) Statistisch-dynamische Analyse skalenabhängiger Niederschlagsprozesse: Vergleich zwischen Beobachtungen und Modell. Dissertation, Freie Universität Berlin
- Claussnitzer A, Névér P (2009) Analysis of quantitative precipitation forecasts using the Dynamic State Index. *Atmos Res* 94(4):694–703. <https://doi.org/10.1016/j.atmosres.2009.08.013>
- Claussnitzer A, Névér P, Langer I, et al (2008) Scale-dependent analyses of precipitation forecasts and cloud properties using the Dynamic State Index. *Meteorol Z* 17(6):813–825. <https://doi.org/10.1127/0941-2948/2008/0346>
- Dagon K, Truesdale J, Biard JC, et al (2022) Machine Learning-Based Detection of Weather Fronts and Associated Extreme Precipitation in Historical and Future Climates. *J Geophys Res: Atmospheres* 127(e2022JD037038). <https://doi.org/10.1029/2022JD037038>
- Eady ET (1949) Long waves and cyclone waves. *Tellus* 1 pp 33–52
- Eliassen A (1962) On the vertical circulation in frontal zones. *Geofys Publikasjoner* 24(4):147–160
- Ertel H (1942) Ein neuer hydrodynamischer Wirbelsatz. *Meteor Z* 59:277–282
- Gaßmann A (2014) Deviations from a general nonlinear wind balance: Local and zonal-mean perspectives. *Meteorol Z* pp 467–481. <https://doi.org/10.1127/metz/2014/0568>
- Gaßmann A (2019) Analysis of large-scale dynamics and gravity waves under shedding of inactive flow components. *Monthly Weather Review* 147(8):2861–2876. <https://doi.org/10.1175/MWR-D-18-0349.1>

- Hewson TD (1998) Objective Fronts. *Meteorol Appl* 5:37–65. <https://doi.org/10.1017/S1350482798000553>
- Hittmeir S, Klein AR, and Müller, Névir P (2021) The dynamic state index with moisture and phase changes. *J Math Phys* 62(123101). <https://doi.org/10.1063/5.0053751>
- Hope P, Keay K, Pook M, et al (2014) A Comparison of Automated Methods of Front Recognition for Climate Studies: A Case Study in Southwest Western Australia. *Mon Weather Rev* 142:343–363. <https://doi.org/10.1175/MWR-D-12-00252.1>
- Hoskins B (1991) Towards a PV- $\theta$  view of the general circulation. *Tellus A: Dynamic Meteorology and Oceanography* 43(4):27–36. <https://doi.org/10.3402/tellusa.v43i4.11936>
- Hoskins B, Pedder M, Jones DW (2003) The omega equation and potential vorticity. *Q J R Meteorol Soc* 129:3277–3303. <https://doi.org/10.1256/qj.02.135>
- Hoskins BJ (1982) The mathematical theory of frontogenesis. *Annu Rev Fluid Mech* 14(1):131–151. <https://doi.org/10.1146/annurev.fl.14.010182.001023>
- Hoskins BJ (1990) Theory of extratropical cyclones. in: *Extratropical cyclones The Erik Palmén Memorial Volume* Eds C Newton and E O Holopainen, American Meteorological Society pp 63–80
- Hoskins BJ, Hodges KI (2002) New perspectives on the Northern Hemisphere winter storm tracks. *J Atmos Sci* 59(6):1041–1061. [https://doi.org/10.1175/1520-0469\(2002\)059<1041:NPOTNH>2.0.CO;2](https://doi.org/10.1175/1520-0469(2002)059<1041:NPOTNH>2.0.CO;2)
- Hoskins BJ, Hodges KI (2005) New perspectives on Southern Hemisphere winter storm tracks. *Journal of Climate* 18:4108–4129. <https://doi.org/10.1175/JCLI3570.1>
- Hoskins BJ, Draghici I, Davies HC (1978) A new look at the omega-equation. *Q J R Meteorol Soc* 104(439):31–38. <https://doi.org/10.1002/qj.49710443903>
- Hoskins BJ, McIntyre ME, Robertson AW (1985) On the use and significance of isentropic potential vorticity maps. *Q J R Meteorol Soc* 111(470):877–945
- Huber-Pock F, Kress C (1981) Contributions to the problem of numerical frontal analysis. *Proceedings of the Symposium on Current Problems of Weather-Prediction*. Vienna, June 23–26, 1981. Publications of the Zentralanstalt für Meteorologie und Geodynamik 253
- Kern M, Hewson T, Schäfler A, et al (2019) Interactive 3D Visual Analysis of Atmospheric Fronts. *IEEE Transactions on Visualization and Computer Graphics* 253. <https://doi.org/10.1109/TVCG.2018.2864806>



- Lange HJ (2002) Die Physik des Wetters und des Klimas: ein Grundkurs zur Theorie des Systems Atmosphäre. Reimer, Berlin
- von Lindheim J, Harikrishnan A, Dörffel T, et al (2021) Definition, detection, and tracking of persistent structures in atmospheric flows. arXiv:2111.13645 <https://doi.org/10.48550/arXiv.2111.13645>
- Mack L (2022) meteoEVT: Computation and Visualization of Energetic and Vortical Atmospheric Quantities, R Package. <https://doi.org/10.32614/CRAN.package.meteoEVT>, URL <https://cran.gedik.edu.tr/web/packages/meteoEVT/meteoEVT.pdf>
- Markowski P, Richardson Y (2010) Mesoscale Meteorology in Midlatitudes. in: Vol 2 of Advancing weather and climate science, 1st Edn., Wiley, Somerset, ISBN 0470742135
- Müller A, Névir P, Klein R (2018) Scale dependent analytical investigation of the dynamic state index concerning the quasi-geostrophic theory. Mathematics of Climate and Weather Forecasting 4(1):1–22. <https://doi.org/10.1515/mcwf-2018-0001>
- Niebler S, Miltenberger A, Schmidt B, et al (2022) Automated detection and classification of synoptic-scale fronts from atmospheric data grids. Weather Clim Dynam 3:113–137. <https://doi.org/10.5194/wcd-3-113-2022>
- Névir P (2004) Ertel’s vorticity theorems, the particle relabelling symmetry and the energy-vorticity theory of fluid mechanics. Meteorol Z 13(6):485–498
- Névir P, Blender R (1993) A Nambu representation of incompressible hydrodynamics using helicity and enstrophy. J Phys A: Math Gen 26(L1189)
- Névir P, Sommer M (2009) Energy–Vorticity Theory of Ideal Fluid Mechanics. J Atmos Sci 66:2073–2084. <https://doi.org/10.1175/2008JAS2897.1>
- Pacey G, Pfahl S, Schielicke L, et al (2023) The climatology and nature of warm-season convective cells in cold-frontal environments over Germany. Nat Hazards Earth Syst Sci 23:3703–3721. <https://doi.org/10.5194/nhess-23-3703-2023>
- Papritz L, Spengler T (2015) Analysis of the slope of isentropic surfaces and its tendencies over the North Atlantic. Q J R Meteorol Soc 141:3226–3238. <https://doi.org/10.1002/qj.2605>
- Parfitt R, Czaja A, Minobe S, et al (2016) The atmospheric frontal response to SST perturbations in the Gulf Stream region. Geophys Res Lett 43:2299–2306. <https://doi.org/10.1002/2016GL067723>
- Parfitt R, Czaja A, Seo H (2017) A simple diagnostic for the detection of atmospheric fronts. Geophys Res Lett 44:4351–4358. <https://doi.org/10.1002/2017GL073662>

- Petterssen S (1936) Contribution to the theory of frontogenesis. *Geofys Publikasjoner* 11(6):1–27
- Pfahl S, O’Gorman PA, Fischer EM (2017) Understanding the regional pattern of projected future changes in extreme precipitation. *Nat Clim change* <https://doi.org/10.1038/NCLIMATE3287>
- R Core Team (2020) R: A Language and Environment for Statistical Computing
- Raveh-Rubin S, Catto JL (2019) Climatology and dynamics of the link between dry intrusions and cold fronts during winter, Part II: Front-centred perspective. *Climate Dynamics* 53:1093–1909. <https://doi.org/10.1007/s00382-019-04793-2>
- Renard RJ, Clarke LC (1965) Experiments and numerical objective frontal analysis. *Monthly Weather Review* 93:547–556. [https://doi.org/10.1175/1520-0493\(1965\)093<0547:EINOFA>2.3.CO;2](https://doi.org/10.1175/1520-0493(1965)093<0547:EINOFA>2.3.CO;2)
- Rossa AM, Wernli H, Davies HC (2000) Growth and Decay of an Extra-Tropical Cyclone’s PV-Tower. *Meteorol Atmos Phys* 73:139–156
- Rudeva I, Simmonds I (2015) Variability and Trends of Global Atmospheric Frontal Activity and Links with Large-Scale Modes of Variability. *J Clim* 28:3311–3330. <https://doi.org/10.1175/JCLI-D-14-00458.1>
- Sawyer JS (1956) The vertical circulation at meteorological fronts and its relation to frontogenesis. *Proc Roy Soc A* 234:346–362
- Schartner T, Névir P, Leckebusch GC, et al (2009) Analysis of Thunderstorms with the Dynamic State Index (DSI) in a Limited Area High Resolution Model. 5th European Conference on Severe Storms
- Schemm S, Sprenger M (2018) When during their life cycle are extratropical cyclones attended by fronts? *Bulletin of the American Meteorological Society* pp 149–166
- Schemm S, Rudeva I, Simmonds I (2015) Extratropical fronts in the lower troposphere–global perspectives obtained from two automated methods. *Q J R Meteorol Soc* 141:1686–1698. <https://doi.org/10.1002/qj.2471>
- Schär C (1993) A generalization of Bernoulli’s theorem. *J Atmos Sci* 50(10):1437–1443. [https://doi.org/10.1175/1520-0469\(1993\)050<1437:AGOBT>2.0.CO;2](https://doi.org/10.1175/1520-0469(1993)050<1437:AGOBT>2.0.CO;2)
- Serreze MC, Lynch AH, Clark MP (2001) The Arctic Frontal Zone as Seen in the NCEP–NCAR Reanalysis. *J Clim* 14:1550–1567. <https://doi.org/10.1175/JCLI-D-14-00458.1>
- Shapiro MA, Keyser D (1990) Fronts, jet streams and the tropopause. *Extratropical Cyclones: The Erik Palmén Memorial Volume*, C Newton and EO Holopainen, Eds, *Amer Meteor Soc* pp 167–191

- Simmonds I, Keay K, Bye JAT (2011) Identification and Climatology of Southern Hemisphere Mobile Fronts in a Modern Reanalysis. *J Climate* 25:1945–1962. <https://doi.org/10.1175/JCLI-D-11-00100.1>
- Soster F, Parfitt R (2022) On Objective Identification of Atmospheric Fronts and Frontal Precipitation in Reanalysis Datasets. *Journal of Climate* 35:4513–4534. <https://doi.org/10.1175/JCLI-D-21-0596.1>
- Spensberger C, Sprenger M (2018) Beyond cold and warm: an objective classification for maritime midlatitude fronts. *Q J R Meteorol Soc* 144:261–277. <https://doi.org/10.1002/qj.3199>
- Steinacker R (1999) Dynamical Aspects of Frontal Analysis. *Meteorol Atmos Phys* 48:93–103
- Tao Z, Xiong Q, Zheng Y, et al (2014) Overview of Advances in Synoptic Meteorology: Four Stages of Development in Conceptual Models of Frontal Cyclones. *Journal of Meteorological Research* 28(5):849–858
- Thomas CM, Schultz DM (2019) Global Climatologies of Fronts, Airmass Boundaries, and Airstream Boundaries: Why the Definition of "Front" Matters. *Monthly Weather Review* 147:691–717. <https://doi.org/10.1175/MWR-D-18-0289.1>
- Uccellini LW, Corfidi SF, Junker NW, et al (1992) Report on the surface analysis workshop held at the National Meteorological Center 25-28 March 1991. *Bull Amer Meteor Soc* 73:459–471
- Volonté A, Clark PA, Gray SL (2018) The role of mesoscale instabilities in the sting-jet dynamics of windstorm Tini. *Q J R Meteorol Soc* 144:877–899. <https://doi.org/10.1002/qj.3264>
- Weber T, Névir P (2008) Storm tracks and cyclone development using the theoretical concept of the Dynamic State Index (DSI). *Tellus A* 60(1):1–10. <https://doi.org/10.1111/j.1600-0870.2007.00272.x>
- Weijenborg C, Friderichs P, Hense A (2015) Organisation of potential vorticity on the mesoscale during deep moist convection. *Tellus A: Dynamic Meteorology and Oceanography* 67(1). <https://doi.org/10.3402/tellusa.v67.25705>
- Wernli H, Davies HC (1997) A Lagrangian-based analysis of extratropical cyclones. I: The method and some applications. *Q J R Meteorol Soc* 123:467–489
- Wernli H, Gray SL (2024) The importance of diabatic processes for the dynamics of synoptic-scale extratropical weather systems – a review. *Weather Clim Dynam* 5:1299–1408. <https://doi.org/10.5194/wcd-5-1299-2024>

Zdunkowski W, Bott A (2003) Dynamics of the Atmosphere. A Course in Theoretical Meteorology. Cambridge University Press, New York